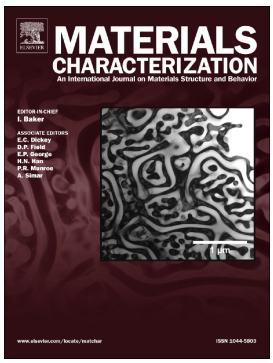

Effect of remelting processes on the microstructure and mechanical behaviours of 18Ni-300 maraging steel manufactured by selective laser melting

Jun Song, Qian Tang, Qixiang Feng, Quanquan Han, Shuai Ma, Hao Chen, Fuyu Guo, Rossitza Setchi

PII: S1044-5803(21)00770-1

DOI: https://doi.org/10.1016/j.matchar.2021.111648

Reference: MTL 111648

To appear in: *Materials Characterization*

Received date: 2 January 2021

Revised date: 20 November 2021

Accepted date: 28 November 2021

Please cite this article as: J. Song, Q. Tang, Q. Feng, et al., Effect of remelting processes on the microstructure and mechanical behaviours of 18Ni-300 maraging steel manufactured by selective laser melting, *Materials Characterization* (2021), https://doi.org/10.1016/j.matchar.2021.111648

Effect of remelting processes on the microstructure and mechanical behaviours of 18Ni-300 maraging steel manufactured by selective laser melting

Jun Song [a], Qian Tang [a], Qixiang Feng [a,*], Quanquan Han [b], Shuai Ma [a], Hao Chen [c], Fuyu Guo [a], Rossitza Setchi [d]

a State Key Laboratory of Mechanical Transmissions, Chongqing University, Chongqing 400044, China

b Key Laboratory of High Efficiency and Clean Mechanical Manufacture of Ministry of Education, Centre for Additive Manufacturing, School of Mechanical Engineering, Shandong University, Jinan 250061, China

c College of Materials Science and Engineering, Chongqing University, Chongqing 400044, China

d Cardiff School of Engineering, Cardiff University, Cardiff CF24 3AA, UK

* Corresponding author: Qixiang Feng

Address: No. 174, Shazheng Street, Shapingba District, Chongqing 400044, China.

Telephone: +8615730306589

E-mail address: fengq2@cqu.edu.cn

Abstract

Selective laser melting (SLM) is an established metal additive manufacturing technology extensively used in the automotive domain to manufacture metallic components with complex structures from 18Ni-300 maraging steel. However, achieving high-performance 18Ni-300 maraging steel using SLM still presents a challenge in terms of formulation of the processing parameters. The remelting process has the potential to address this challenge during SLM before post-treatments. This paper systematically investigated the effect of remelting on the microstructure and mechanical behaviours of the SLM-built 18Ni-300 maraging steel. The experimental results suggest that increases in the relative density of the as-built samples from 99.12 % to 99.93 % are achieved by a specific combination of remelting parameters (laser power 200 W, scan speed 750 mm/s, remelting rotation 90° and hatch spacing

0.11 mm) that eliminate large-sized pores. Compared with the as-built condition, remelting can slightly coarsen the average grain sizes and increased the fraction of low-angle grain boundaries (2°–15°). The tensile strength showed no remelting dependence, whereas both the ductility and microhardness increased. Elongation of the as-built sample increased from 10.5 ± 0.8 % to 13 ± 3.5 % after remelting under the #28 condition. These findings provide a fundamentally new understanding of how a combination of SLM and remelting can aid in the manufacture of high-performing 18Ni-300 maraging steel.

Keywords: Selective laser melting; Maraging steel; Remelting; Microstructure; Mechanical behaviour

1. Introduction

Additive manufacturing (AM) technologies have received widespread attention in the last few decades, and they are now widely applied in numerous modern industries. One laser powder bed AM process, termed selective laser melting (SLM), is used to build complex 3D metallic products directly from raw materials in a layer-by-layer manner [1]. Compared to conventional manufacturing methods, SLM processing is less time consuming, has a shorter production cycle and wastes less material [2]. Moreover, the high cooling rates formed during SLM generate final components with a refined microstructure that can further enhance their mechanical properties [3]. Extensive studies have demonstrated many successful fabrications of metallic parts using SLM processing in high-value sectors, including the aerospace, automotive and medical device industries. At present, many metallic products have been successfully manufactured by SLM from raw powder materials, such as Ti-6Al-4V [4] and stainless steel [5]. However, despite the clear benefits of SLM, the high complexity of this process creates difficulties in optimising the process parameters. For this reason, SLM technology is not yet fully understood or fully exploited.

SLM is recognised as having significant processing potential, but several issues

remain that hinder its use. One issue involves the relative density of the final products, as this can be detrimental to the final performance. In general, previous studies have shown that some newly introduced materials employed for SLM processing can achieve a full relative density (higher than 99%) through careful selection of the process parameters, such as the laser power, scanning speed, hatch spacing, layer thickness and scanning strategy. For example, Croteau et al. [6] achieved crack-free Al-Mg-Zr alloy samples with laser energy densities of 123–247 J/mm^3 and a relative density of over 99.2 %. Similarly, Mao et al. [7] studied the process optimisation of a Cu-15Sn alloy using a response surface method and reported that the samples with the highest relative density of 99.6 % were achieved under the optimal parameter conditions. Various other studies have also focused on alloy-based composites and the addition of nanoparticles. For example, Han et al. [8] explored methods for fabricating crack-free Hastelloy X parts using SLM and found that microcracks were eliminated from the samples by introducing 1 wt.% titanium carbide nanoparticles into the raw Hastelloy X powder particles. Nevertheless, several residual pores were still observed in the samples.

In general, as-built samples with a relative density lower than 100 % are thought to possess internal defects, such as residual metallurgical pores and microcracks, and these issues actually cannot be resolved by SLM process optimisation. Cai et al. employed the hot isostatic pressing technology to manufacture parts directly from raw metallic powders, and they achieved almost full dense parts with excellent mechanical behaviours [9, 10]. In addition, this technology is regarded as an effective post-treatment approach for the porosity closure within SLM-built samples [11]. However, this processing can also degrade the tensile strength, and the heat treatment can cause a reappearance of porosity in the samples [12].

A more promising approach is laser remelting, which is a process that scans the same layer and melts it twice (or multiple times) with the same laser source before spreading a new powder layer. Yasa et al. [13] explored the feasibility of remelting each layer to perfect the relative density and surface roughness of 316L and Ti6Al4V

and demonstrated that remelting could improve the density and enhance the surface roughness. The increased processing time for the remelting process limited the initial studies on laser remelting; however, recent studies have indicated a renewed interest in its potential for practical applications. For example, Griffiths et al. [14] studied the effect of single and multiple remelting of each layer on the microstructure of Al-Mg-Zr alloy during SLM and found that remelting contributed to a refinement of the microstructure.

Wei et al. [15] showed that the top surface roughness of a Ti-5Al-2.5Sn alloy could be reduced by increasing the number of remelting cycles, whereas the side surface roughness could not be improved. Nevertheless, remelting improved the ductility while keeping the same level of tensile strength seen in the as-built samples. Yu et al. [16] studied the porosity distribution of the AlSi10Mg samples by employing two remelting strategies (in the same and opposite directions to the first melting). Their microcomputed tomography (micro-CT) results revealed that both remelting strategies reduced the pores in the central regions to the same extent; however, remelting in the same direction also decreased in the pores at the edges. The authors adopted the same process parameters with powder melting, but did not consider the effects of other process parameters.

One material that may be suitable for SLM is 18Ni-300 maraging steel, a workhorse material that exhibits high strength and ductility and has been widely implemented in diverse applications, such as automatic moulding domains [17]. In recent years, several researchers have studied both the process optimisations of this material fabricated using SLM and the effect of heat treatments on the microstructure and mechanical behaviours [18, 19]. For example, Casalino et al. [20] studied the correlation between the energy density and relative density of SLM-fabricated 18Ni-300 maraging steel. The authors found that the relative density increased with the increase in energy density, and they manufactured samples with a relative density higher than 99%. Bodziak et al. [21] studied the effects of ageing at 510 °C for 2 h on SLM-built samples and found that pores and microcracks were not eliminated

efficiently by this treatment. Casati et al. [22] studied the effect of different ageing conditions on the tensile strength of SLM-built 18Ni-300 maraging steel and found that a solution treatment was not required before the samples were subjected to ageing. However, Tan et al. [23] suggested that a combination of solution and ageing treatments was more desirable for SLM maraging steel. Song et al. [24] and Mutua et al. [25] studied the tensile anisotropic behaviour of samples in as-built and heat-treated conditions, and all the three groups found a lower tensile strength for vertically fabricated samples than for horizontally fabricated ones. Bai et al. [26] found that higher elongation and impact property were obtained in the samples fabricated with 45 deg build directions.

Recently, Cao et al. [27] studied the effect of support structures on the dimensional accuracy, hardness, and surface quality of SLM-built 18Ni-300 maraging steel at different build angles. The authors found the more accurate quality and higher microhardness for samples built with support structures than without. Bai et al. [28] investigated the effect of process parameters on surface quality and internal porosity of SLM-built 18Ni-300 maraging steel and determined that the top surfaces were smoother at lower scan speed and layer thickness and that the best surface was obtained at a layer thickness of 20 μm. Wang et al. [29] designed a novel alloying composition of 18Ni-300 maraging steel and studied the process parameters, microstructure and mechanical behaviours of this steel fabricated by SLM. They obtained a simultaneous enhancement of strength and elongation after the as-built samples were subjected to ageing treatment.

However, none of these previous studies considered the remelting process of the samples. Some studies have used remelting, but no consensus has been reached regarding the relationships between the remelting process and the microstructure and mechanical properties of 18Ni-300 maraging steel. In general, the effect of SLM processing on 18Ni-300 maraging steel is still underexplored. For this reason, this study aimed to evaluate the feasibility of using the remelting processing with SLM-built 18Ni-300 maraging steel samples and to conduct a systematic investigation

of the effect of remelting on the density, microstructure and mechanical behaviours. The overall goal is to develop the potential of SLM processing and to provide practical advice for employing SLM and remelting combinations for the production of high-quality 18Ni-300 maraging steel parts.

2. Materials and Experimental Methods

2.1 Materials and processing

18Ni-300 maraging steel powder prepared by gas atomisation was used as the raw material for the SLM process in the present study. Fig. 1a and b show the powder particle morphology of the 18Ni-300 maraging steel at low and high magnifications, respectively, as observed by scanning electron microscopy (SEM; JEOL JSM-7800F FEG, Japan). Most particles were spherical. Fig. 1c shows a cross-section of the powder and the micropores trapped in the powder particles. Fig. 1d shows the particle size distribution of the powder, as measured with a Mastersizer (Microtrac S3500). The D10, D50 and D90 values of the powder were 18.19 μm, 29.11 μm and 48.64 μm, respectively. Table 1 shows the alloying composition (wt.%) of the 18Ni-300 maraging steel powder used in this study, which was measured by inductively coupled plasma optical emission spectroscopy (ICP-OES, Agilent 5110, USA).

Table 1 The alloying composition of the 18Ni-300 maraging steel powder.

Element	Ni	Co	Mo	Ti	Al	Mn	Si	P	S	C	Fe
(wt.%)	19.06	9.07	4.12	0.5	0.16	0.03	0.22	0.01	0.09	<0.03	Bal.

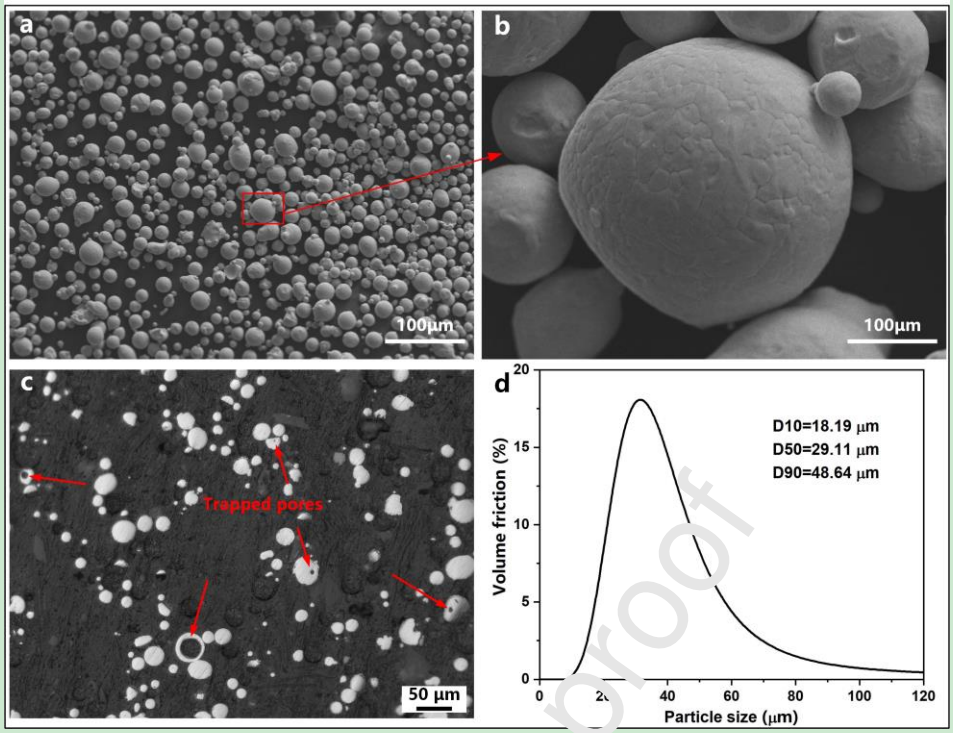

Fig. 1. 18Ni-300 maraging steel powder used in this study: (a-b) surface morphology; (c) cross-section morphology and (d) particle size distribution.

In this study, both SLM and the remelting processes were conducted on a metallic SLM apparatus (EP-M 250, E-plus 3D Technology Ltd., China) equipped with a maximum laser power of 500 W and capable of a maximum scanning speed of 2000 mm/s. Two cubic samples with dimensions of 8 × 8 × 8 mm^3 were prepared for each processing condition on a 304 stainless steel build plate. The plate was not preheated before the fabrication. The build chamber was filled with a nitrogen atmosphere, with the oxygen content below 0.6%. The process parameter group for the as-built condition used in this study was selected as follows: laser power of 285 W, scan speed of 900 mm/s, hatching space of 0.11 mm and layer thickness of 0.04 mm. In this study, the as-built samples were the samples without remelting. A discontinuous, short, bidirectional scanning strategy was used, and the scanning direction was rotated at 320°, 336°, 352°, 8°, 24° and 40° between successive layers. Fig. 2 shows the schematic diagram of the processing with and without remelting and remelting. No contour strategy was applied for the cubic samples during either the

SLM or remelting processing. To maintain the dimension accuracy of the tensile samples compared to the standard dimension, a contour strategy was employed.

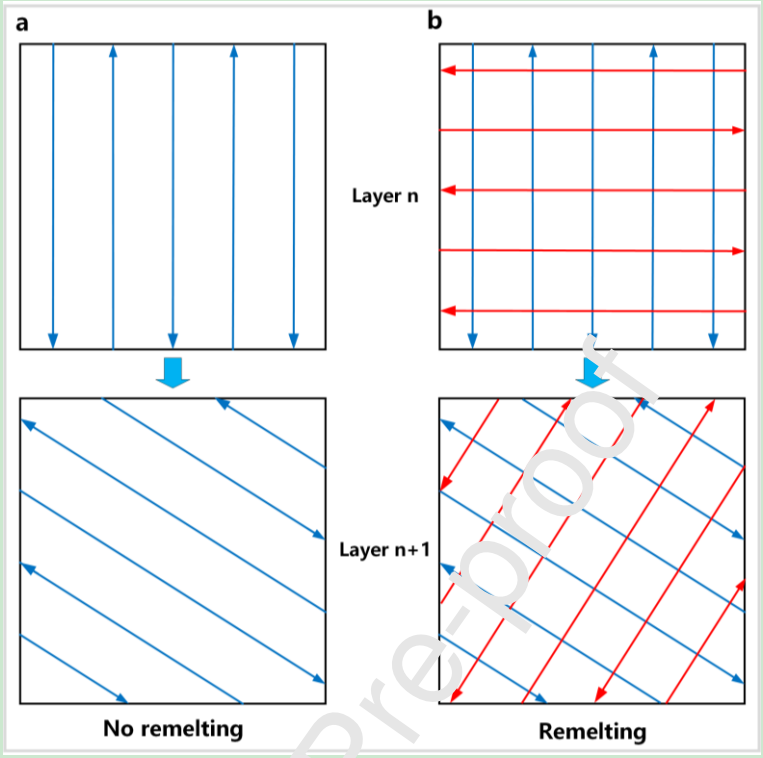

Fig. 2. Schematic diagram of the processing (a) with no remelting and (b) with remelting. The blue and red lines represent the first and second scanning tracks during remelting, respectively.

Only one remelting step was implemented in this study. The remelting parameters, including the laser power, scan speed, hatch spacing and remelting rotation, were varied to determine their effects on relative density and defects. The physical properties of solid materials differ from those of powders; therefore, the process parameters for the remelting process should also be considered. The remelting process parameters used are shown in Table 2.

Table 2 The range of matrix remelting process parameters used in this study.

Parameters	Level 1	Level 2	Level 3	Level 4	Level 5
Laser power (W)	150	175	200	225	250
Scan speed (mm/s)	550	650	750	850	950
Remelting rotation (°)	0	45	90	135	180
Hatch spacing (mm)	0.11	0.12	0.13	0.14	0.15

2.2 Experimental methods

The design of the experiment included the response surface method (RSM), as it is a useful approach for understanding the effect of the interaction of remelting parameters on the performance of the fabrication. Therefore, RSM was adopted to optimise remelting process parameters. Minitab 17 software was used to design, analyse and evaluate the relationship between the remelting process parameters and the relative density. The detailed combinations of remelting parameters based on the RSM are shown in Table 3. Variance analysis was performed in previous studies to correlate the process parameters with relative density when employing the design of experiments [30, 31]. The present study aimed to achieve huge datasets that could provide insight into the effects of various remelting parameter combinations on the sample microstructure and mechanical behaviour.

Table 3 Experimental design matrix of the remelting parameters designed by RSM.

Sample number	Laser power (W)	Scan speed (mm/s)	Remelting rotation (°)	Hatch spacing (mm)
#1	200	750	180	0.13
#2	175	650	45	0.12
#3	200	550	90	0.13
#4	200	750	90	0.13
#5	175	650	135	0.12
#6	225	850	45	0.12
#7	175	650	45	0.14
#8	200	950	90	0.13
#9	175	850	45	0.14
#10	200	750	90	0.13
#11	225	850	45	0.14
#12	225	650	135	0.12
#13	225	650	45	0.12
#14	200	750	90	0.13
#15	225	650	135	0.14
#16	175	850	135	0.14
#17	250	750	90	0.13
#18	200	750	90	0.13

#19	175	650	135	0.14
#20	150	750	90	0.13
#21	175	850	45	0.12
#22	200	750	0	0.13
#23	200	750	90	0.13
#24	200	750	90	0.13
#25	200	750	90	0.15
#26	225	650	45	0.14
#27	175	850	135	0.12
#28	200	750	90	0.11
#29	225	850	135	0.12
#30	225	850	135	0.14

2.3 Material characterisation techniques

The support structures of all samples were removed, and the samples were then ultrasonically cleaned for ten minutes before density measurements. The density was measured by the Archimedes method using an HZY-A120 electronic balance. A minimum of five measurements for each sample was obtained to calculate the average density. X-ray microCT (diondo d2, Germany) characterisation at 120 kV voltage and 80 µA was used to investigate the effect of process parameters on the porosity distribution within the as-built and remelted samples. Samples were vertically sectioned, ground up and then mirror polished by standard processing before microstructure observations.

The defects formed along the build direction were observed by optical microscopy (OM; Keyence VHX-1000 digital microscope). To reveal the molten pool boundaries and solidification microstructures, the polished samples were then etched using a reagent consisting of 25 ml HNO_3, 50 ml HCl, 1 g $CuCl_2$, and 150 ml water before OM and SEM observations. Phase measurements were conducted on a SmartLab X-ray diffraction (XRD) diffractometer using CuKα radiation at 40 kV and 40 mA, with a scan speed of 2°/min and a step size of 0.02°. Electron backscatter diffraction (EBSD) analysis was determined by SEM using the JEOL JSM-7800F instrument at 20 kV with a step size of 0.65 µm. The experimental data were analysed using the HKL-EBSD Channel 5 software package.

Uniaxial tensile testing was conducted at room temperature using an MTS landmark servohydraulic testing system with a strain rate of 0.05 min^{-1}. Before testing, the gauge, each sample was subjected to proper mechanical polishing. For each parameter combination, at least two counterparts were used for testing. The fracture morphology of the tested samples was also characterised by SEM using the JEOL JSM-7800F instrument. The Vickers microhardness (HV) on the side surface was determined using a Zwick tester at a constant load of 500 g with a dwell time of 8 s. Ten random points were tested to achieve the average values.

3. Results and Discussion

3.1 Density and porosity analysis

Fig. 3a shows the measured relative density of the samples under different remelting conditions. The blue dashed line represents the relative density of the as-built sample and had a value of 99.12% under the as-built processing condition. However, the sample with the lowest relative density of 98.16% was fabricated with the #2 remelting conditions. The #28 sample had the highest relative density, at 99.93%, with the remelting process parameters of laser power, scan speed, remelting rotation and hatch spacing of 200 W, 750 mm/s, 90° and 0.11 mm, respectively. This increasing trend in relative density could be attributed to two possible reasons. One was that the improved surface quality during the remelting process could result in a uniform spreading of the powder to be recoated [13]. The other was that remelting could eliminate defects, such as large-sized pores and microcracks, within the sample. Fig. 3b shows the main effects plot for the relative density versus remelting processing parameters. The remelting rotation showed variation in values but it contributed only trivially to the relative density in the present study.

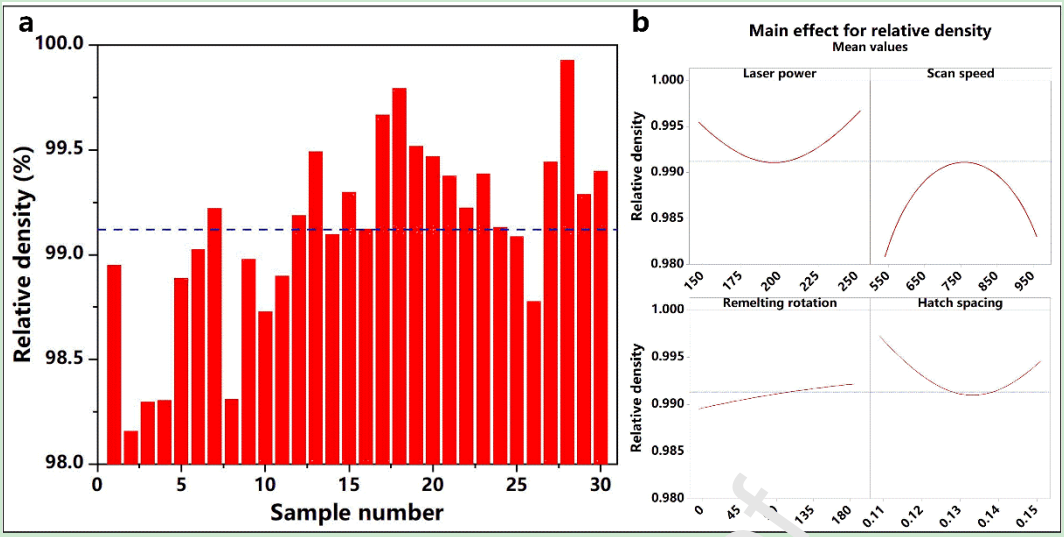

Fig. 3. Relative density in various processing conditions: (a) relative density measured by the Archimedes method; (b) main effects for the relative density versus remelting processing parameters.

Fig. 4a-f show optical micrographs of the porosity distributions along vertical sections of the as-built sample and five remelted samples (#2; #3; #16; #18 and #28 samples). Notably, no significant correlation could be observed between the remelting energy density and the relative density amongst these five samples. Gustmann et al. [32] also found a similar result in their study on remelting of a Cu-Al-Ni-Mn shape-memory alloy. As shown in Fig. 4a, both spherical and irregular shaped pores were evident in the as-built sample; these represented typical defects formed in SLM-fabricated parts. The spherical pores were categorised as metallurgical micropores and were mainly attributed to gas entrapped within the feedstock powder particles and the shielding gas in the samples during processing [33].

The formation of irregularly shaped pores primarily resulted from insufficient laser energy input. Fig. 4b-f show that defects, such as irregular-shaped pores, spherical pores, and microcracks, formed in the samples following the application of different remelting conditions. For the #2 and #28 samples, despite the use of similar laser power, entirely different pores were formed as the scan speed was varied (Fig. 4b and f). The #2 sample showed irregularly shaped pores with a larger size than observed in the as-built sample, whereas very few micropores with spherical shapes were formed in the #28 sample. This result showed that porosity formation was highly susceptible to the scan speed during remelting.

In general, pore movements are simultaneously controlled by thermocapillary force and drag force during the laser process, and these are induced by the temperature gradient and Marangoni-driven melt flow, respectively [34, 35]. The higher cooling rates create a steeper temperature gradient during remelting compared with the as-built condition. Therefore, a much stronger thermocapillary force can be generated during remelting, and this becomes the dominating driving force that controls the pore activity. This driving force contributes to the movement of the irregularly shaped pores along the temperature gradient within the molten pools and then escapes from them [34]. The solidified layer was also remelted during the remelting process, and the large-sized metallurgical micropores were dispersed with the melted liquid metals [36]. This could explain the irregularly shaped pore elimination and the increased numbers of gas pores observed in the #28 sample. However, for the #2 sample, these irregularly shaped pores were freshly formed during remelting due to the suboptimal parameter selection, and the pores differed from those formed in the as-built sample. The main reason for this difference could be that a lower scan speed caused the molten pools to persist for a longer duration. Thus, the shielding gas could be drawn into the molten pools due to the stronger molten pool activity [37].

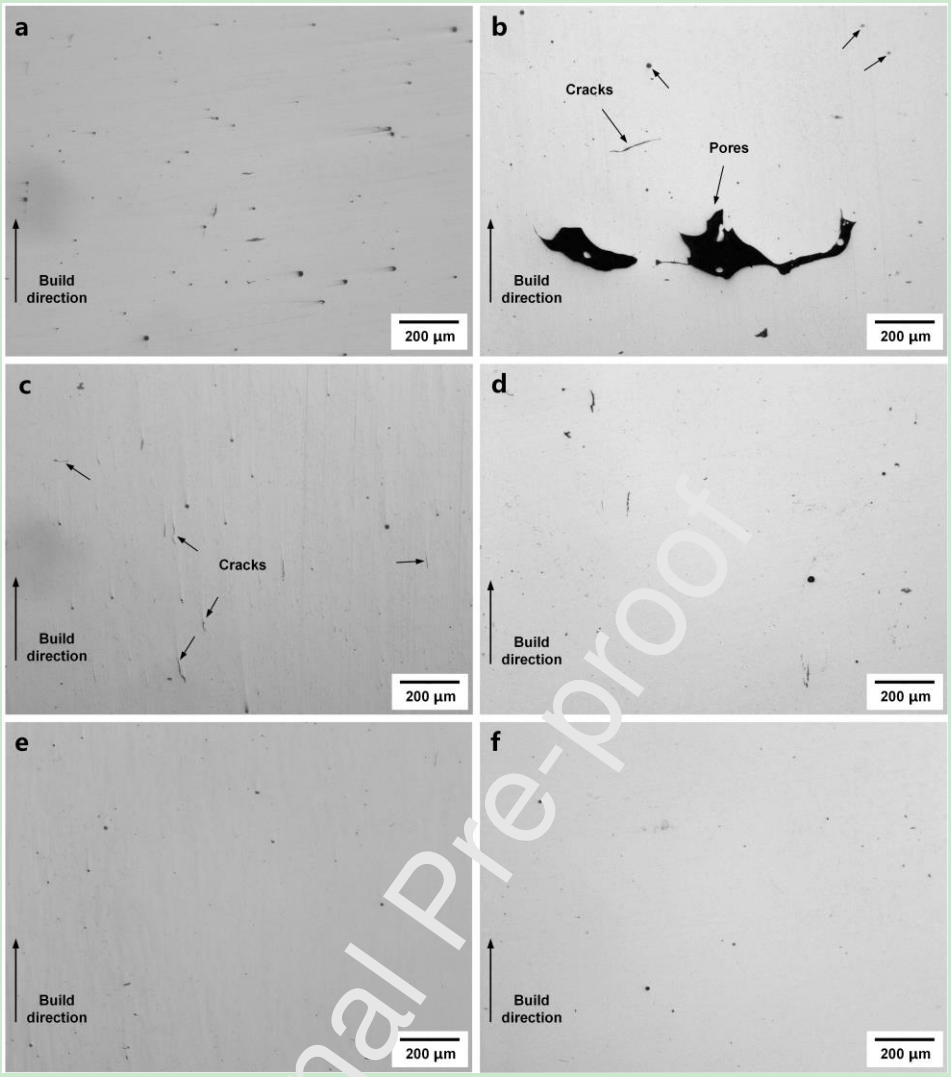

Fig. 4. Optical micrographs showing the defects in the vertical sections of the as-built and remelted samples: (a) as-built; (b) #2 (P = 175 W, v = 650 mm/s, R = 45° and h = 0.12 mm); (c) #3 (P = 200 W, v = 550 mm/s, R = 90° and h = 0.13 mm); (d) #16 (P = 175 W, v = 850 mm/s, R = 135° and h = 0.14 mm); (e) #18 (P = 200 W, v = 750 mm/s, R = 90° and h = 0.13 mm); and (f) #28 (P = 200 W, v = 750 mm/s, R = 90° and h = 0.11 mm). P, v, R and h represent laser power, scan speed, remelting rotation and hatch spacing during remelting, respectively.

Fig. 5 shows the reconstructed porosity distributions and pore equivalent diameter versus frequency of the as-built, #2 and #28 samples. The micro-CT measurements revealed a small number of pores within the as-built sample (Fig. 5a),

thereby confirming the high measured relative density; approximately 441 pores were detected with a bulk volume of 0.058 mm^3. However, a large number of irregularly shaped and elongated pores were observed in the #2 sample (Fig. 5b), where the pore numbers and bulk volume were 976 and 1.57 mm^3, respectively. These analyses could account for the lower relative density of the sample. The pore quantity in the #28 sample was slightly increased compared to the as-built sample (512, based on the micro-CT examination); however, this increase was accompanied by an overall decrease in the pore volume, with a value of 0.047 mm^3 (Fig. 5c). Larger-sized pores were eliminated within the #28 sample, particularly in the intermediate regions, and the overall pore size was smaller than in the as-built sample, in agreement with both the relative density measurement and the OM observation.

Pores were also detected near the edge regions along the side surfaces, within these three samples, as is commonly observed when employing a discontinuous scanning strategy. These pores could be a result of the formation and subsequent collapse of deep keyhole depressions induced by the deceleration and acceleration of the laser beam during the laser turn points [38]. Similar observations were reported by du Plessis and le Roux in their experiments using a round-robin test [39].

Fig. 5d and e show the equivalent diameter versus porosity frequency within the three samples. The micro-CT data indicated an average pore diameter of 80 μm and a maximum pore size within the as-built sample of 445 μm. The pores ranging from 25 to 100 μm in equivalent diameters within the as-built sample and #28 sample (Fig. 5e) reached accumulated frequencies of 95.24% and 98.83%, respectively; no pores larger than 200 μm in equivalent diameters were observed. However, Fig. 5e also shows that the number of pores ranging from 25 to 100 μm in equivalent diameters slightly increased within the #28 sample compared to the number present in the as-built sample. The extent of the increase in these pores may be associated with the formation of gas and keyhole porosities during remelting. Large pores (100–200 μm in equivalent diameters) also decreased significantly in the #28 sample, confirming that large pores could be eliminated by employing the #28 remelting condition.

However, for the #2 sample, the accumulated frequency of the pores ranging from 25 to 100 μm in equivalent diameters was only 76.54% (Fig. 5d). In addition, a large number of large pores with equivalent diameters of over 100 μm were detected, and the accumulated frequency of small, medium and large pores reached a value of 92.11%.

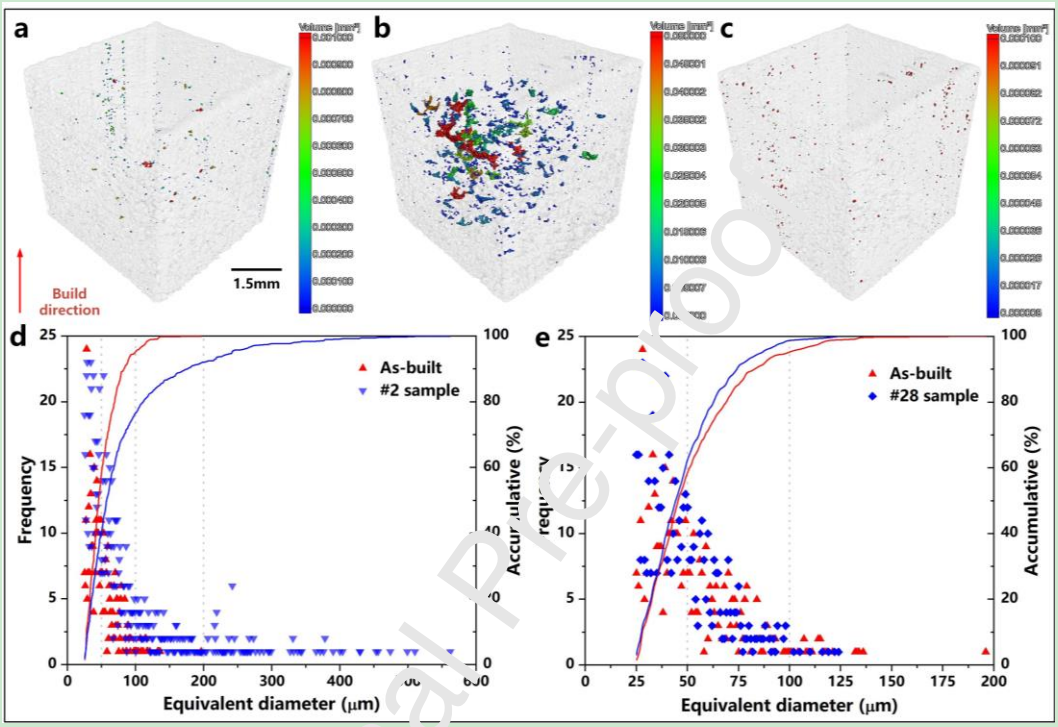

Fig. 5. Micro-CT reconstructed pore distributions of (a) as-built; (b) #2; and (c) #28 samples; and (d-e) pore equivalent diameter versus frequency in the three samples.

3.2 Microstructure

Fig. 6 shows OM micrographs of the molten pool boundaries and defects in the as-built and remelted samples. Several defects, such as irregular and residual pores, were observed in the as-built sample (Fig. 6a). Most molten pools exhibited uniform semi-elliptical shapes, indicating that the conduction mode was dominant under the optimised processing condition. Compared with the as-built sample, the samples exhibited different molten pool morphologies under different remelting conditions (Fig. 6b–f). The dimensions of the molten pools in the remelted samples were smaller than those of the as-built sample, indicating that the molten pools were only partially melted during remelting. This difference was because the bulk materials had higher

and more uniform thermal conductivity than the raw powder materials [16]. Both irregular and residual pores were observed in #2 and #3 samples, which also showed irregular molten pool distributions (Fig. 6b and c).

The shapes of the molten pools shown in Fig. 6d–f were uniform, while several molten pools in samples #16 and #18 exhibited a greater depth. Samples #18 and #28 showed similar molten pool widths and heights (Fig. 6e and f). This similarity occurred because these two samples were built using the same laser power, scan speed and remelting rotation; therefore, similar tracks were formed during processing. The distance between the two scanning tracks was larger in the #18 sample than in the #28 sample. This was due to the larger hatch spacing of the #18 sample. Moreover, compared to the as-built and #2 samples, more residual pores were observed in the remelting fusion boundaries in the #28 sample. This detection was consistent with the micro-CT observations.

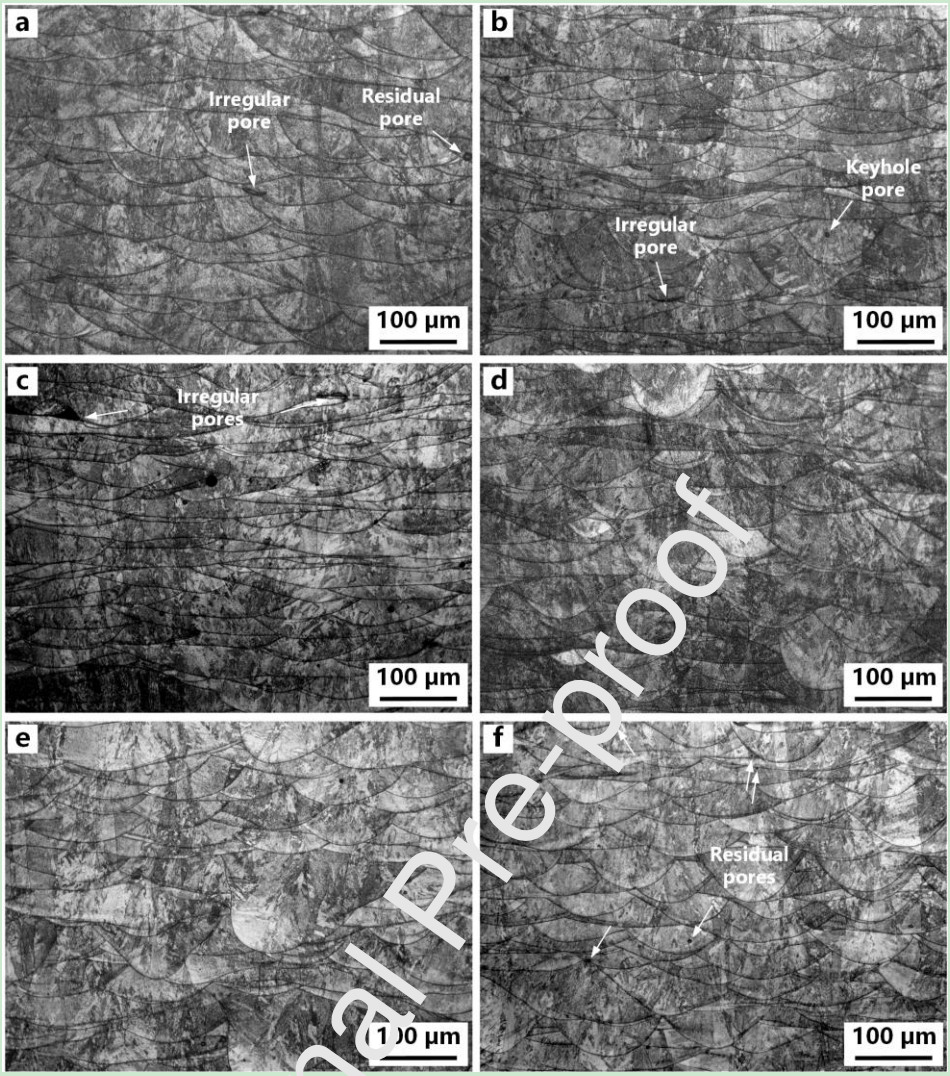

Fig. 6. Optical micrographs showing the molten pools in the as-built and different remelting conditions: (a) as-built; (b) #2; (c) #3; (d) #16; (e)#18; and (f) #28 samples.

Fig. 7 shows SEM micrographs of the fusion boundaries and solidification structures of the as-built and remelted samples. As shown in the low-magnification micrographs in Fig. 7a–c and g–i, both cellular and columnar grains were observed in the as-built and remelted samples. Due to the nature of the SLM process, this typical heterogeneous microstructure was determined by the thermal gradient and solidification rate under the as-built and remelting conditions [40]. Microcracks propagating along the build direction were observed in the samples shown in Fig. 7c, g and h, indicating that under these process parameter combinations, remelting led to the formation of microcracks or failed to effectively suppress them.

As shown in the higher magnification micrographs in Fig. 7d–f and j–l,

solidification structures were observed in more detail in the molten pools. In general, columnar grains grew towards the centre of the molten pools along the build direction, and some grew through several molten pools. The growth direction of columnar grains in the as-built sample did not always follow this rule because of the rotation scan strategy employed between successive layers (Fig. 6d). Cellular grains are also formed in molten pools. However, it seems that the remelting rotation resulted in a more irregular direction of columnar grains and a more random distribution of cellular grains in the remelted samples. Moreover, due to the higher thermal gradient and solidification rate during remelting, the size of the cellular grains in some regions of the remelted samples was smaller than in the as-built samples. Chen et al. [41] also reported similar observations when remelting an AlSi10Mg composite.

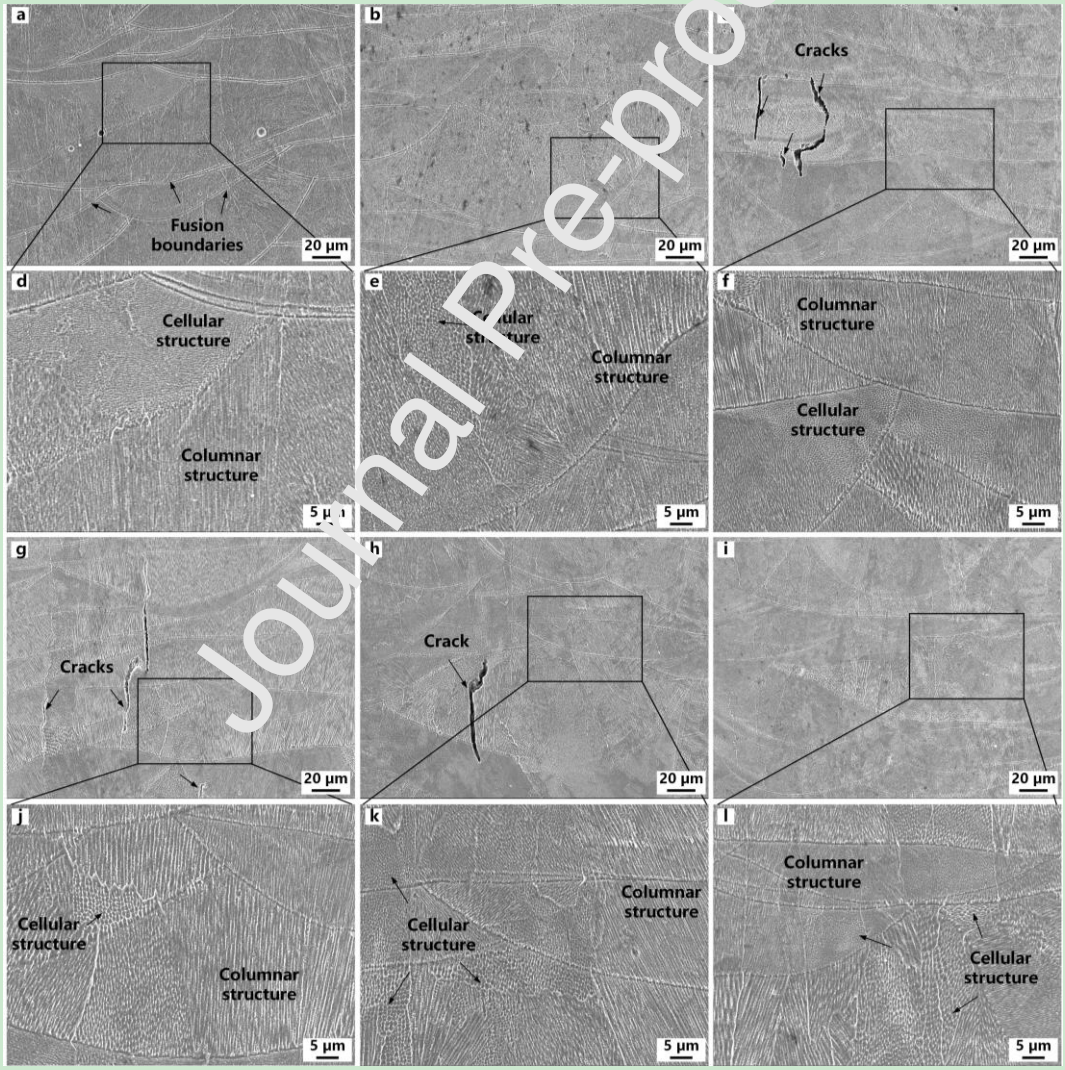

Fig. 7. SEM micrographs showing the solidification structures in as-built and remelted samples under different remelting conditions: (a, d) as-built; (b, e) #2; (c, f)

#3; (g, j) #16; (h, k) #18; and (i, l) #28 samples.

Fig. 8 shows the XRD patterns of the 18Ni-300 maraging steel powder and the samples under the as-built and different remelting conditions. The major phase in the powder and samples was the martensite (α) phase, and the corresponding peaks were attributed to (110), (200) and (211), these peaks were detected in both the powder and the samples (Fig. 8a). This observation is consistent with the results reported in previous studies [1, 23]. The peaks corresponding to the austenite (γ) phase were particularly low in the samples, indicating that only a small number of γ phases were formed. The quick heat dissipation rate during processing could be responsible for this observation.

As heat treatment methods are effective at inducing phase changes, Tan et al. [23] showed that the γ phase was completely transformed into an α phase by a 1 h solution treatment of an SLM-built 18Ni 300 maraging steel sample at 840 °C. No obviously different intensity values were observed between the as-built and remelted samples, while the 2θ angles of the peaks of the as-built sample were shifted to lower values following remelting (Fig. 8). Bragg's Law shows that decreases in 2θ values would result in increased distances between adjacent lattice planes. This was correlated with the lattice distortion induced by thermal stress during remelting [42].

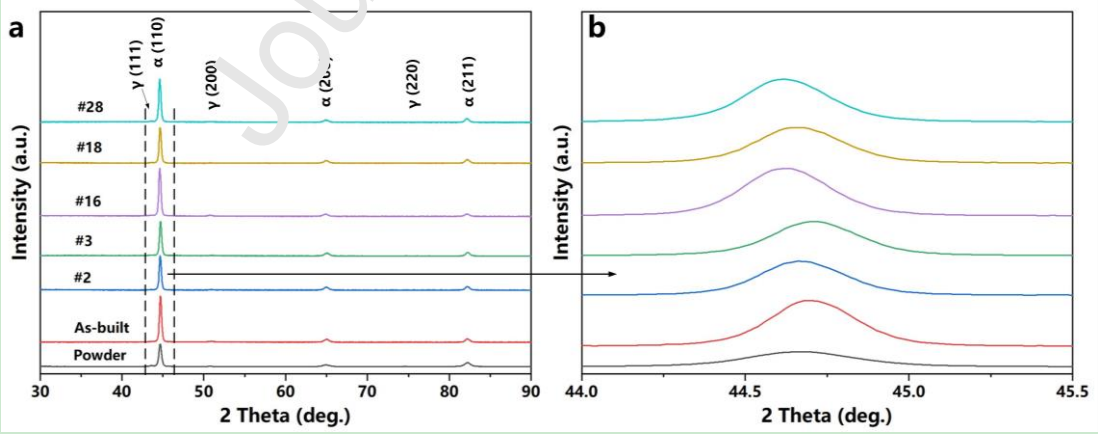

Fig. 8. XRD patterns of the 18Ni-300 maraging steel powder feedstock and the samples fabricated under the as-built and different remelting conditions.

Fig. 9 shows the EBSD inverse pole figure (IPF) micrographs and grain size distributions of the aspect ratios along the build direction (BD), corresponding to the samples fabricated under the as-built, #16 and #28 conditions. Elongated columnar microstructures were the major features for the as-built, #16 and #28 samples, while a small number of equiaxed grains with sizes of hundreds of nanometres were also observed (Fig. 9a–c). These equiaxed grains were always formed inside or at the boundaries of the columnar grains. The IPF colour distributions revealed no obvious preferred grain orientation for the three samples; this was probably a result of the complex heat transfer induced by the rotations between adjacent layers during the SLM and remelting process. In general, columnar microstructures grow preferentially along the <100> direction in cubic crystal structures [43]. During laser processing, the directions of the heat flow and cooling play a major role in the formation of the microstructure for both the as-built and remelted samples. The formed microstructure was associated with the distribution of thermal gradients within the molten pools along the BD during the SLM and remelting processes [44].

Fig. 9d shows no significant differences for the aspect ratio distribution of the grains in the samples. The calculated grain numbers based on the IPF micrographs were 2632, 2007 and 2521 for the as-built, #16 and #28 samples, respectively. The aspect ratio percentage significantly decreased with an increase in the aspect ratio of the grains for each sample. Roughly 53% of the grains had an aspect ratio of less than 2. Based on the statistical data, a threshold grain area of 8.45 μm^2 was used to calculate the equivalent diameter of each grain in the samples. The measured average grain sizes were 6.1 μm, 6.9 μm and 6.3 μm, respectively, in the as-built, #16 and #28 samples. These results indicated that remelting tended to create a slightly coarsened microstructure under either low or high energy density. Gustmann et al. [32] also found that higher remelting energy input coarsened the grain sizes of the Cu-Al-Ni-Mn shape-memory alloy samples.

In general, the thermal conductivity was higher for the solid material than for the powder material; therefore, heat dissipated more quickly during remelting. This

rapid cooling rate is favourable for grain refinement [45]; however, the heat-affected zones introduced by remelting can also result in coarsening of the grains and grain recrystallisation in the solidified regions [14]. This could be the dominant factor that determined the coarsening microstructure after remelting. In addition, the smaller grain size in the #28 sample than in the #16 sample suggested that the employed remelting rotation of 90° may more efficiently destroy the columnar grains while also contributing to the formation of equiaxed grains.

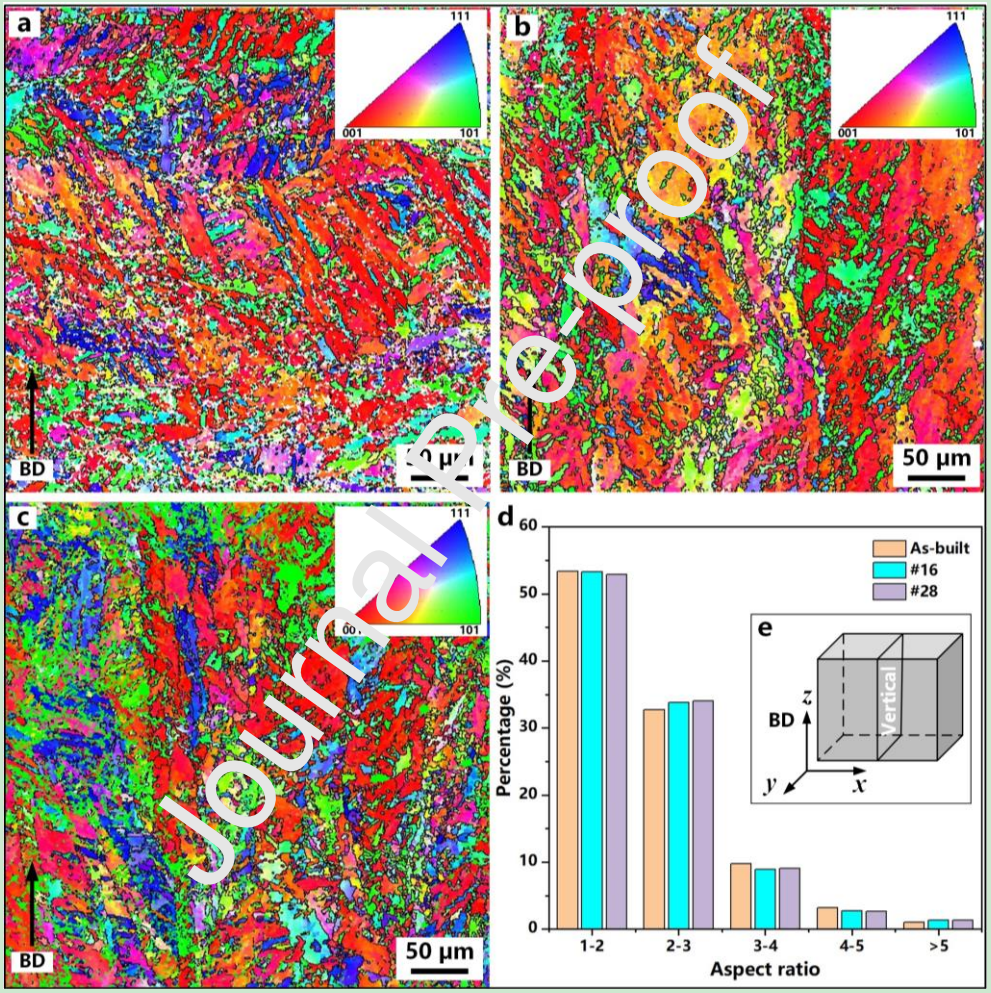

Fig. 9. EBSD crystallographic orientation maps of (a) as-built; (b) #16; (c) #28 samples; (d) aspect ratio distribution of the grains in all the samples; and (e) schematic of the sample coordinate direction.

Fig. 10 shows the corresponding pole figure (PF) maps of the three samples. As shown in Fig. 10a, the as-built sample achieved the maximum texture intensity value

of 3.82, while the remelting processing weakened the crystal texture of the sample. As depicted in Fig. 10b-c, the maximum texture intensity values were 3.32 and 3.16 for the #16 sample and #28 sample, respectively. Therefore, the remelting processing with rotation decreases the texture level in the current cases. This decrease in the texture levels in both remelted samples could be associated with the rotation between the powder melting and remelting. Although the #16 sample and #28 sample exhibited differences in their energy densities, only the scanning directions of the laser beam plays a significant role in determining the formations of texture. In particular, texture decreases significantly with a rotation of 90° between neighbouring layers. Future studies will focus on the effect of the remelting scanning directions on the microstructures.

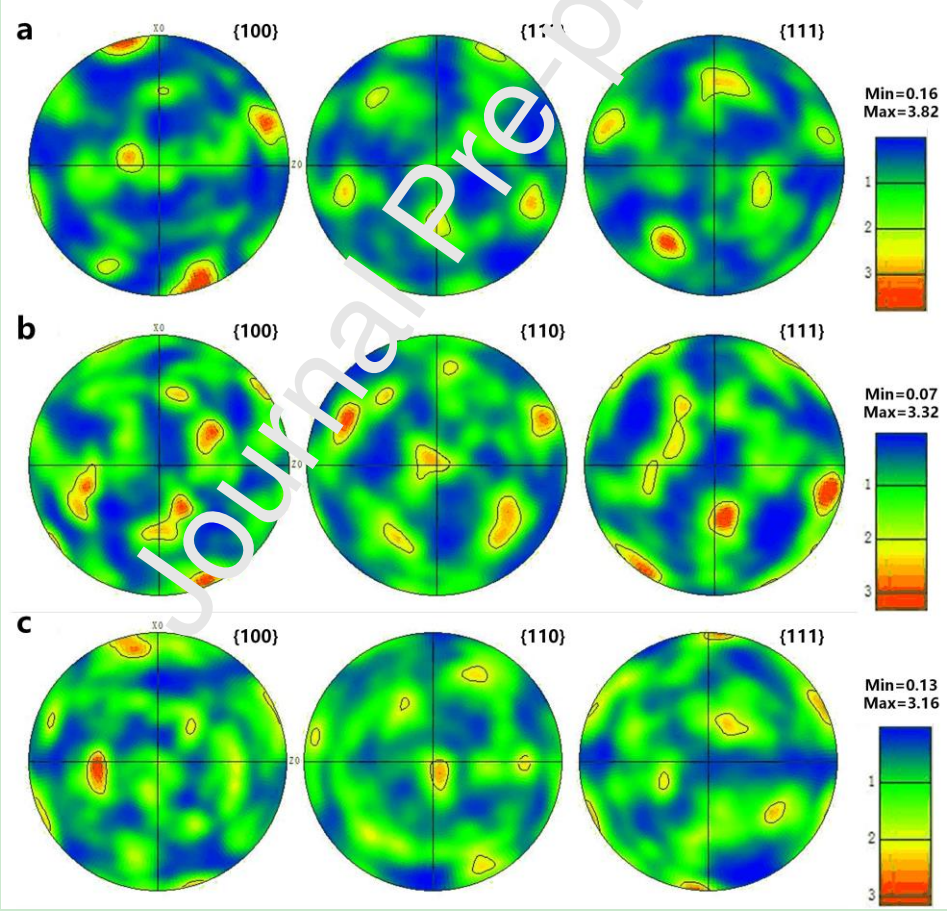

Fig. 10. Pole figure maps showing the crystal textures of the (a) as-built; (b) #16; (c) #28 samples.

Fig. 11a–c show the high-magnification grain boundary maps for the samples, with low angle grain boundaries (LAGBs, 2°–15°) and high angle grain boundaries (HAGBs, >15°) presented as blue and red lines, respectively. Fig. 11d–f shows the misorientation angle distributions of the LAGBs and HAGBs for the three samples, based on the EBSD IPF measurements shown in Fig. 9. Our measurements revealed the presence of a large percentage of LAGBs in all three samples. The as-built sample contained a fraction of LAGBs with a value of 60.4 % (Fig. 11d), while the fraction of LAGBs was considerably increased to 67.5 % and 64.2 % in the #16 and #28 samples, respectively (Fig. 11e and f). This large fraction of LAGBs could be attributed to the formation of subgrains and cellular microstructures induced by the rapid cooling rate during the SLM and remelting process [46]. The greater number of reheating and cooling cycles during remelting led to a slightly higher content of LAGBs in the #16 and #28 samples than was observed in the as-built sample. This result could be the more formation of small-sized nanoprecipitates induced by the intrinsic heat treatment effect during remelting, since the movement of dislocations can be blocked by these nanoprecipitates [20].

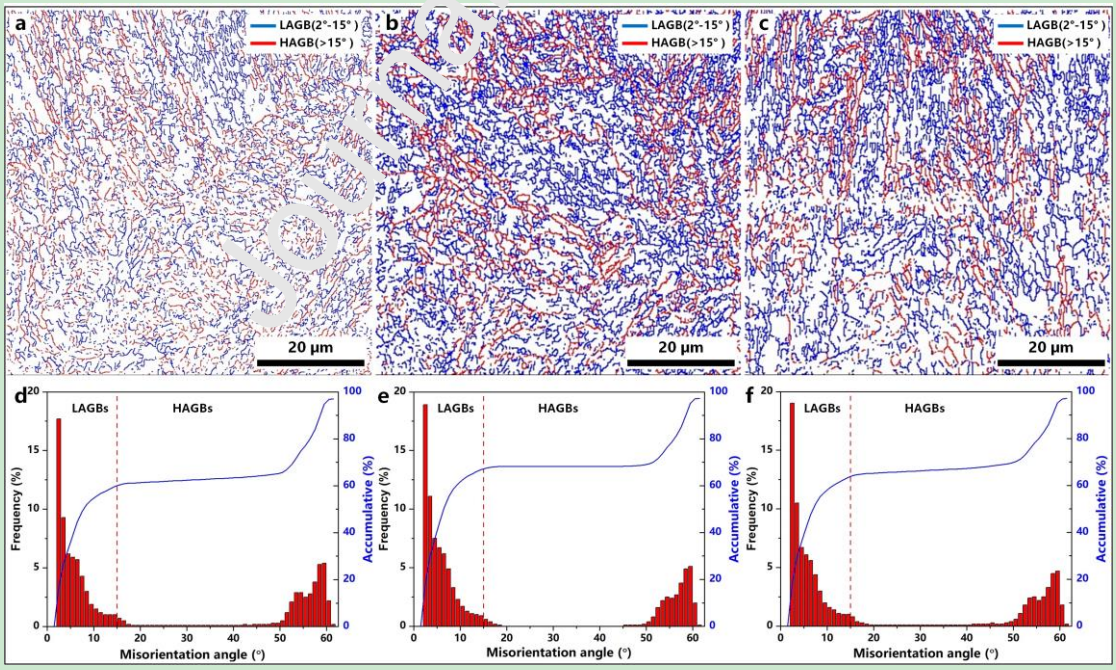

Fig. 11. EBSD photographs showing the grain boundary maps and misorientation angle distributions for (a, d) as-built; (b, e) #16; (c, f) #28 samples.

3.3 Mechanical behaviours

Fig. 12 shows the tensile behaviours of the samples under the as-built and different remelting conditions following uniaxial tensile testing measured at room temperature. Note that the #3 tensile samples in the present study failed to be fabricated due to the high energy density input during remelting. The typical stress-strain curves for the five processing conditions and tensile sample dimensions are shown in Fig. 12a, while Fig. 12b shows the summary of the yield strength (YS), ultimate tensile strength (UTS) and elongation. The as-built samples had a YS of 1030 ± 17 MPa, a UTS of 1084 ± 15 MPa and an elongation of 10.5 ± 0.8 %. Compared to the as-built samples, the quantitative results revealed no apparent differences when comparing the YS and UTS of the samples in the four remelting conditions. Amongst the remelting conditions, the #28 samples had the highest relative density, resulting in a YS and UTS of 1022 ± 8 MPa and 1083 ± 13 MPa, respectively. The relative density measurements indicated that the pore volume may not have an obviously significant role in tensile properties despite the slight difference in relative density.

The elongation, however, was quite different in the remelting versus the as-built samples. The #2 samples, with the lowest relative density, also had the lowest elongation of 4.82 + 0.9 % amongst the five processing conditions. Despite the similar relative density, the elongation of the #16 samples slightly decreased to 9 ± 1 %. This decrease could be explained by the OM observations, which revealed a large number of microcracks. The elongation was improved to 11 ± 1.1 % and 13 ± 3.5 % for the #18 and #28 samples, respectively. The greatest elongation amongst the three #28 samples was 16.5 %.

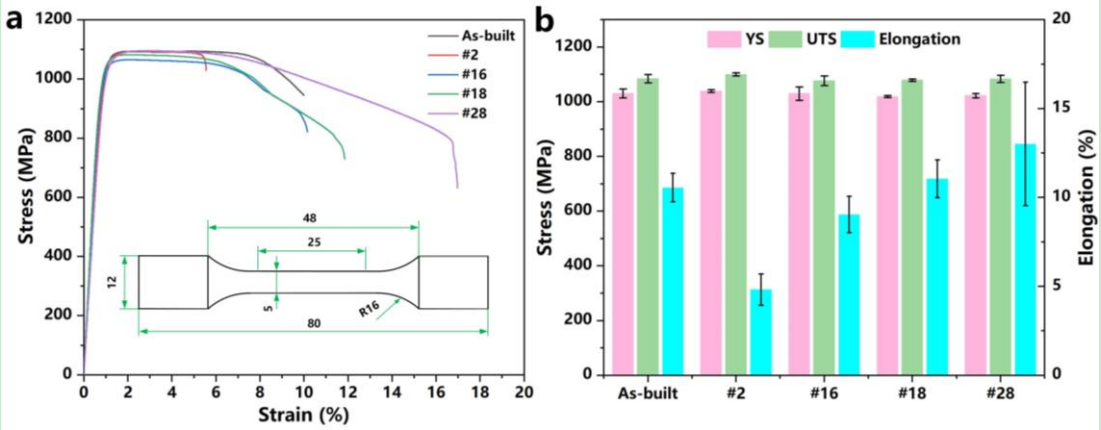

Fig. 12. Uniaxial tensile testing results of the samples under the as-built and remelting conditions: (a) Stress-strain curves; (b) summary of the YS, UTS and elongation.

Fig. 13 shows the SEM morphologies of the fracture surfaces for the as-built, #2 and #28 samples following tensile testing. The as-built sample contained a large number of microcracks and pores, as determined from its fracture morphology (Fig. 13a and b). Some unmelted powder particles were also observed and were always entrapped inside the pores. By contrast, the #28 samples showed only limited pores and microcracks in their fracture morphology, as shown in Fig. 13d and e. When viewed at high magnification, the fracture morphologies revealed a large number of dimple-like microstructures, indicating a similar ductile fracture for both sample types (Fig. 13c and f). The dimples in both samples were smaller than 1 μm in size, whereas the dimples were deeper in the #28 samples than in the as-built samples, implying better ductile behaviour in the #28 samples. These observations could explain the enhanced performance in elongation compared with the as-built samples. Fig. 13g and h show the fracture morphology of the #2 sample, which shows a large number of pores and cracks and a flatter fracture morphology feature compared to the as-built and #28 samples (Fig. 13a and d). Both observations could explain the resulting decrease in elongation behaviour.

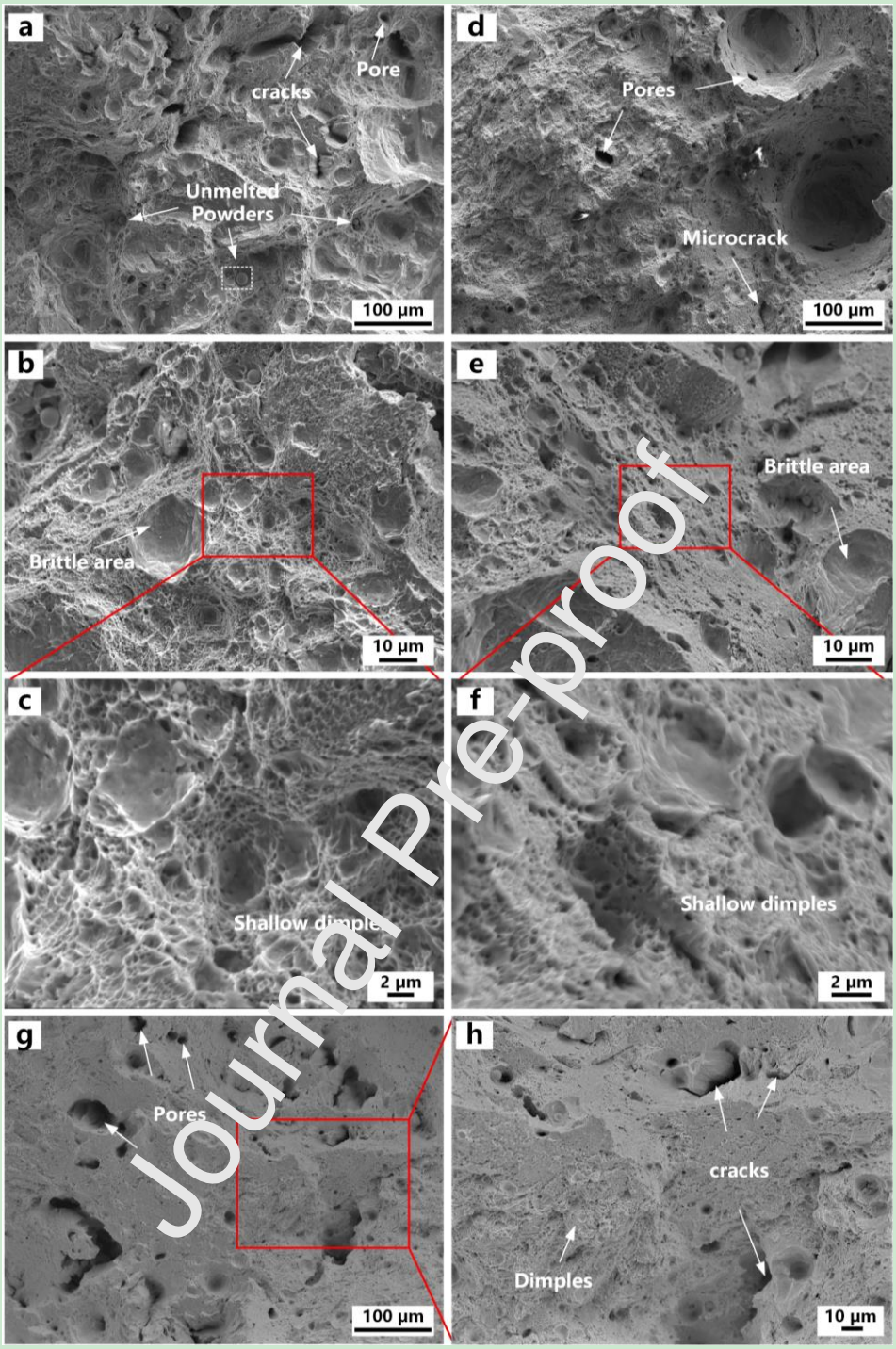

Fig. 13. Scanning electron microscopy micrographs showing the fracture surfaces of the (a–c) as-built; (d–f) #28; and (g–h) #2 samples at different magnifications.

Fig. 14 shows the Vickers microhardness results for tests on the polished side surfaces of the as-built and remelted samples. The as-built sample had an average microhardness value of 345 ± 10 HV, whereas the microhardness values of the

samples in different remelting conditions ranged from 350 ± 3 to 362 ± 4 HV. These values indicated that slightly higher microhardness values were achieved after remelting compared to the as-built condition. In addition, among the five remelted samples, the hardness value showed a slight decrease with increases in the energy density input.

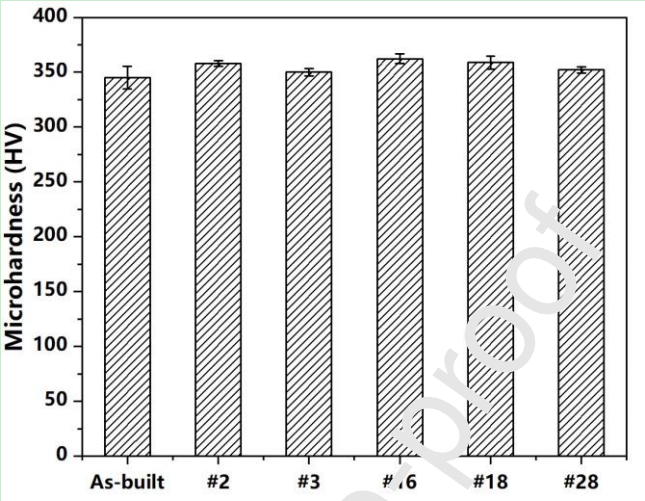

Fig. 14. Vickers microhardness measurements on the side surfaces of the as-built sample and remelted samples in different conditions.

3.4 Strengthening mechanisms

Enhanced mechanical behaviours are commonly attributed to several possible strengthening mechanisms, including grain refinement, high dislocation density and nanoprecipitate formation [47]. The Hall-Petch effect predicts that the high strength is related to the fine microstructure [48]. In this study, the EBSD results indicated no significant change in the grain sizes after remelting compared with the as-built sample (Fig. 9). In addition, the dislocation density quantitatively calculated from the XRD results ranged between $2.53 \times 10^{14}/m^2$ and $2.76 \times 10^{14}/m^2$, indicating that no obvious difference between the as-built and remelted samples (Fig. 15). Therefore, both of these strengthening mechanisms could be ignored as explanations for the change in strength and ductility observed in our study.

During laser additive manufacturing of 18Ni-300 maraging steel, an intrinsic heat treatment effect is commonly observed under the as-built condition, and this effect contributes to a massive formation of nanoprecipitate in the metal matrix [23, 49]. In the present study, remelting allowed the solidified tracks and layers to undergo

more reheating and cooling cycles, which could have resulted in the formation of more nanoprecipitates than occurred in the as-built condition. Based on the analysis, this could be the main contributor to the slightly enhanced hardness seen after remelting. In addition to enhanced ductility, the elongation was improved with increases in relative density after remelting. Two factors could explain this finding. First, remelting of the as-built sample can eliminate the large-sized pores, which significantly influenced the elongation behaviour. Second, the formation possibility of more nanoprecipitates in the metal matrix during remelting could promote dislocation plasticity, thereby enhancing ductility [50].

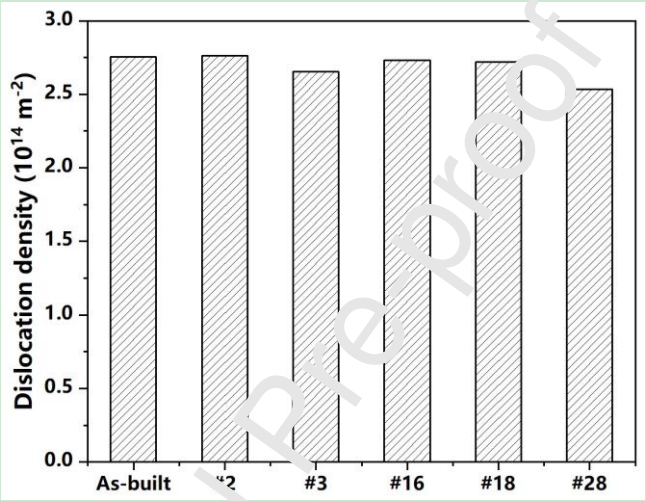

Fig. 15. The estimated dislocation density of the samples in as-built and remelting conditions.

4. Conclusions

This study was a systematic investigation of the effects of various remelting parameters on the relative density and porosity distribution of 18Ni-300 maraging steel samples manufactured by SLM. The corresponding microstructure and mechanical behaviours of the samples in the as-built and remelting conditions were also examined. The important conclusions are summarised as follows:

(1) The relative density of the as-built samples was increased from 99.12% to 99.93% in the remelted samples fabricated using a laser power of 200 W, a scan speed of 750 mm/s, a remelting rotation of 90° and a hatch spacing of 0.11 mm. Employment of the processing conditions described here improved the density by modifying the surface qualities to promote subsequent powder

spreading and simultaneous elimination of defects that formed in the as-built condition. The micro-CT observations confirmed that remelting could noticeably reduce the large-sized pores in the as-built sample, but this occurred at the expense of increased numbers of gas and keyhole pores. However, remelting played no crucial role in the formation of pores close to the side surfaces due to the employed discontinuous scanning strategy.

(2) The formation of a large percentage of α phase was the dominating phase in both as-built and remelting conditions, and no obvious difference in phase was observed after remelting. EBSD observations showed that remelting slightly coarsened the average grain sizes and contributed to an increased amount of LAGBs. The amount of LAGBs in the as-built condition was 60.4 % and increased to 67.5 % and 64.2 % in the #16 and #28 conditions, respectively.

(3) Compared to the as-built samples, no significant changes were noted in yield strength and ultimate tensile strength for the samples fabricated under various remelting conditions. However, the elongation of the #28 sample noticeably increased from 10.5 ± 0.8 % to 13 ± 3.5 %. The possible strengthening mechanism was the reduced number of large pores within the samples after remelting and the formation of more nanoprecipitates induced by an intrinsic heat treatment effect. Smaller sized dimples were also observed in the #28 sample compared to the as-built samples, indicating better ductile behaviour of the sample in the #28 remelting condition. A slight improvement in hardness was observed after remelting.

In summary, this study provides a fundamentally new understanding of the influences of different remelting conditions on the formation quality, microstructure and tensile performance of 18Ni-300 maraging steel fabricated by SLM. This study is significant since it provides useful guidance for enhancing the relative density and ductility of as-built 18Ni-300 maraging steel parts by employing combined SLM and remelting processing in practical applications. Notably, the described procedure eliminates the need for post-treatment. Future work will focus on the effects of various remelting conditions on the fatigue performance of 18Ni-300 maraging steel

samples.

Data availability

The raw/processed data required to reproduce these findings cannot be shared at this time as the data also forms part of an ongoing study.

Acknowledgements

This paper was supported by the Natural Science Foundation of China (Grant No: 51975073, 51805052, 52005295), Graduate Research and Innovation Foundation of Chongqing (No. CYB18019). The authors also express their appreciation for the help from the Electron Microscopy Centre of Chongqing University (China) regarding the observation of the microstructure and fracture morphology. The lead author (Jun Song) gratefully acknowledges the financial support from China Scholarship Council (CSC).

References

[1] K. Kempen, E. Yasa, L. Thijs, J.P. Kruth, J. Van Humbeeck, Microstructure and mechanical properties of selective laser melted 18Ni-300 steel, Phys. Procedia. 12 (2011) 255–263. https://doi.org/10.1016/j.phpro.2011.03.033.

[2] N.T. Aboulkhair, N.M. Everitt, I. Ashcroft, C. Tuck, Reducing porosity in AlSi10Mg parts processed by selective laser melting, Addit. Manuf. 1 (2014) 77–86. https://doi.org/10.1016/j.addma.2014.08.001.

[3] B. AlMangour, D. Grzesiak, J.M. Yang, Scanning strategies for texture and anisotropy tailoring during selective laser melting of TiC/316L stainless steel nanocomposites, J. Alloys Compd. 728 (2017) 424–435. https://doi.org/10.1016/j.jallcom.2017.08.022.

[4] Q. Feng, Q. Tang, Y. Liu, R. Setchi, S. Soe, S. Ma, L. Bai, Quasi-static analysis of mechanical properties of Ti6Al4V lattice structures manufactured using selective laser melting, Int. J. Adv. Manuf. Technol. 94 (2018) 2301–2313. https://doi.org/10.1007/s00170-017-0932-7.

[5] S. Ma, Q. Tang, X. Han, Q. Feng, J. Song, R. Setchi, Y. Liu, Y. Liu, Manufacturability, Mechanical Properties, Mass-Transport Properties and Biocompatibility of Triply Periodic Minimal Surface (TPMS) Porous Scaffolds Fabricated by Selective Laser Melting, Mater. Des. 195 (2020) 109034. https://doi.org/10.1016/j.matdes.2020.109034.

[6] J.R. Croteau, S. Griffiths, M.D. Rossell, C. Leinenbach, C. Kenel, V. Jansen, D.N. Seidman, D.C. Dunand, N.Q. Vo, Microstructure and mechanical properties of Al-Mg-Zr alloys processed by selective laser melting, Acta Mater. 153 (2018) 35–44. https://doi.org/10.1016/j.actamat.2018.04.053.

[7] Z. Mao, D.Z. Zhang, J. Jiang, G. Fu, P. Zhang, Processing optimisation, mechanical properties and microstructural evolution during selective laser melting of Cu-15Sn high-tin bronze, Mater.

Sci. Eng. A. 721 (2018) 125–134. https://doi.org/10.1016/j.msea.2018.02.051.

[8] Q. Han, Y. Gu, R. Setchi, F. Lacan, R. Johnston, S.L. Evans, S. Yang, Additive manufacturing of high-strength crack-free Ni-based Hastelloy X superalloy, Addit. Manuf. 30 (2019) 100919. https://doi.org/10.1016/j.addma.2019.100919.

[9] C. Cai, S. He, L. Li, Q. Teng, B. Song, C. Yan, Q. Wei, Y. Shi, In-situ TiB/Ti-6Al-4V composites with a tailored architecture produced by hot isostatic pressing: Microstructure evolution, enhanced tensile properties and strengthening mechanisms, Compos. Part B Eng. 164 (2019) 546–558. https://doi.org/10.1016/j.compositesb.2019.01.080.

[10] C. Cai, X. Gao, Q. Teng, R. Kiran, J. Liu, Q. Wei, Y. Shi, Hot isostatic pressing of a near α-Ti alloy: Temperature optimization, microstructural evolution and mechanical performance evaluation, Mater. Sci. Eng. A. 802 (2021) 140426. https://doi.org/10.1016/j.msea.2020.140426.

[11] Q. Han, R. Mertens, M.L. Montero-Sistiaga, S. Yang, R. Setchi, K. Vanmeensel, B. Van Hooreweder, S.L. Evans, H. Fan, Laser powder bed fusion of Hastelloy X: Effects of hot isostatic pressing and the hot cracking mechanism, Mater. Sci. Eng. A. 732 (2018) 228–239. https://doi.org/10.1016/j.msea.2018.07.008.

[12] S. Tammas-Williams, P.J. Withers, I. Todd, P.B. Prangnell, Porosity regrowth during heat treatment of hot isostatically pressed additively manufactured titanium components, Scr. Mater. 122 (2016) 72–76. https://doi.org/10.1016/j.scriptamat.2016.05.002.

[13] E. Yasa, J. Deckers, J.P. Kruth, The investigation of the influence of laser re-melting on density, surface quality and microstructure of selective laser melting parts, Rapid Prototyp. J. 17 (2011) 312–327. https://doi.org/10.1108/13552541111156450.

[14] S. Griffiths, M.D. Rossell, J. Croteau, N.Q. Vo, D.C. Dunand, C. Leinenbach, Effect of laser rescanning on the grain microstructure of a selective laser melted Al-Mg-Zr alloy, Mater. Charact. 143 (2018) 34–42. https://doi.org/10.1016/j.matchar.2018.03.033.

[15] K. Wei, M. Lv, X. Zeng, Z. Xiao, C. Huang, M. Liu, J. Deng, Effect of laser remelting on deposition quality, residual stress, microstructure, and mechanical property of selective laser melting processed Ti-5Al-2.5Sn alloy, Mater. Charact. 150 (2019) 67 – 77. https://doi.org/10.1016/j.matchar.2019.02.010.

[16] W. Yu, S.L. Sing, C.X. Chua, X. Tian, Influence of re-melting on surface roughness and porosity of AlSi10Mg parts fabricated by selective laser melting, J. Alloys Compd. 792 (2019) 574–581. https://doi.org/10.1016/j.jallcom.2019.04.017.

[17] R. Branco, J.D. Costa, J.A. Martins Ferreira, C. Capela, F. V. Antunes, W. Macek, Multiaxial fatigue behaviour of maraging steel produced by selective laser melting, Mater. Des. 201 (2021) 109469. https://doi.org/10.1016/j.matdes.2021.109469.

[18] Z. Li, B. Teng, B. Yao, J. Liu, Microstructure and mechanical properties of WC reinforced 18Ni300 composites produced by selective laser melting, Mater. Charact. 180 (2021) 111406. https://doi.org/10.1016/j.matchar.2021.111406.

[19] Y. Bai, Y. Yang, D. Wang, M. Zhang, Influence mechanism of parameters process and mechanical properties evolution mechanism of maraging steel 300 by selective laser melting, Mater. Sci. Eng. A. 703 (2017) 116–123. https://doi.org/10.1016/j.msea.2017.06.033.

[20] G. Casalino, S.L. Campanelli, N. Contuzzi, A.D. Ludovico, Experimental investigation and statistical optimisation of the selective laser melting process of a maraging steel, Opt. Laser

Technol. 65 (2015) 151–158. https://doi.org/10.1016/j.optlastec.2014.07.021.

[21] S. Bodziak, K.S. Al-Rubaie, L.D. Valentina, F.H. Lafratta, E.C. Santos, A.M. Zanatta, Y. Chen, Precipitation in 300 grade maraging steel built by selective laser melting: Aging at 510 °C for 2 h, Mater. Charact. 151 (2019) 73–83. https://doi.org/10.1016/j.matchar.2019.02.033.

[22] R. Casati, J.N. Lemke, A. Tuissi, M. Vedani, Aging behaviour and mechanical performance of 18-Ni 300 steel processed by selective laser melting, Metals (Basel). 6 (2016) 218. https://doi.org/10.3390/met6090218.

[23] C. Tan, K. Zhou, W. Ma, P. Zhang, M. Liu, T. Kuang, Microstructural evolution, nanoprecipitation behavior and mechanical properties of selective laser melted high-performance grade 300 maraging steel, Mater. Des. 134 (2017) 23–34. https://doi.org/10.1016/j.matdes.2017.08.026.

[24] J. Song, Q. Tang, Q. Feng, S. Ma, R. Setchi, Y. Liu, Q. Han, Y. Fan, M. Zhang, Effect of heat treatment on microstructure and mechanical behaviours of 18Ni-300 maraging steel manufactured by selective laser melting, Opt. Laser Technol. 120 (2019) 105725. https://doi.org/10.1016/j.optlastec.2019.105725.

[25] J. Mutua, S. Nakata, T. Onda, Z.C. Chen, Optimization of selective laser melting parameters and influence of post heat treatment on microstructure and mechanical properties of maraging steel, Mater. Des. 139 (2018) 486–497. https://doi.org/10.1016/j.matdes.2017.11.042.

[26] Y. Bai, Y.J. Lee, C. Li, H. Wang, Densification Behavior and Influence of Building Direction on High Anisotropy in Selective Laser Melting of High-Strength 18Ni-Co-Mo-Ti Maraging Steel, Metall. Mater. Trans. A Phys. Metall. Mater. Sci. 51 (2020) 5861–5879. https://doi.org/10.1007/s11661-020-05974-9.

[27] Q. Cao, J. Zhang, S. Chang, J.Y.H. Fuh, X. Wang, The effect of support structures on maraging steel MS1 parts fabricated by selective laser melting at different building angles, Rapid Prototyp. J. 26 (2020) 1465–1476. https://doi.org/10.1108/RPJ-11-2019-0287.

[28] Y. Bai, C. Zhao, D. Wang, J. Wang, Evolution mechanism of surface morphology and internal hole defect of 18Ni300 maraging steel fabricated by selective laser melting, J. Mater. Process. Technol. 299 (2022) 117328. https://doi.org/10.1016/j.jmatprotec.2021.117328.

[29] Y. Wang, L. Luo, T. Liu, B. Wang, L. Luo, J. Zhao, L. Wang, Y. Su, J. Guo, H. Fu, Tuning process parameters to optimize microstructure and mechanical properties of novel maraging steel fabricated by selective laser melting, Mater. Sci. Eng. A. 823 (2021) 141740. https://doi.org/10.1016/j.msea.2021.141740.

[30] G. Miranda, S. Faria, F. Bartolomeu, E. Pinto, N. Alves, N. Peixinho, M. Gasik, F.S. Silva, A study on the production of thin-walled Ti6Al4V parts by selective laser melting, J. Manuf. Process. 39 (2019) 346–355. https://doi.org/10.1016/j.jmapro.2018.12.036.

[31] M. Yakout, M.A. Elbestawi, S.C. Veldhuis, Density and mechanical properties in selective laser melting of Invar 36 and stainless steel 316L, J. Mater. Process. Technol. 266 (2019) 397–420. https://doi.org/10.1016/j.jmatprotec.2018.11.006.

[32] T. Gustmann, H. Schwab, U. Kühn, S. Pauly, Selective laser remelting of an additively manufactured Cu-Al-Ni-Mn shape-memory alloy, Mater. Des. 153 (2018) 129–138. https://doi.org/10.1016/j.matdes.2018.05.010.

[33] C. Cai, C. Radoslaw, J. Zhang, Q. Yan, S. Wen, B. Song, Y. Shi, In-situ preparation and formation of TiB/Ti-6Al-4V nanocomposite via laser additive manufacturing: Microstructure

evolution and tribological behavior, Powder Technol. 342 (2019) 73–84. https://doi.org/10.1016/j.powtec.2018.09.088.

[34] S.M.H. Hojjatzadeh, N.D. Parab, W. Yan, Q. Guo, L. Xiong, C. Zhao, M. Qu, L.I. Escano, X. Xiao, K. Fezzaa, W. Everhart, T. Sun, L. Chen, Pore elimination mechanisms during 3D printing of metals, Nat. Commun. 10 (2019) 1–8. https://doi.org/10.1038/s41467-019-10973-9.

[35] S.A. Khairallah, A.T. Anderson, A. Rubenchik, W.E. King, Laser powder-bed fusion additive manufacturing: Physics of complex melt flow and formation mechanisms of pores, spatter, and denudation zones, Acta Mater. 108 (2016) 36–45. https://doi.org/10.1016/j.actamat.2016.02.014.

[36] C.L.A. Leung, S. Marussi, R.C. Atwood, M. Towrie, P.J. Withers, P.D. Lee, In situ X-ray imaging of defect and molten pool dynamics in laser additive manufacturing, Nat. Commun. 9 (2018) 1–9. https://doi.org/10.1038/s41467-018-03734-7.

[37] F. Lv, H. Liang, D. Xie, Y. Mao, C. Wang, L. Shen, Z. Tian, On the role of laser in situ re-melting into pore elimination of Ti–6Al–4V components fabricated by selective laser melting, J. Alloys Compd. 854 (2021) 156866. https://doi.org/10.1016/j.jallcom.2020.156866.

[38] A.A. Martin, N.P. Calta, S.A. Khairallah, J. Wang, P.J. Depond, A.Y. Fong, V. Thampy, G.M. Guss, A.M. Kiss, K.H. Stone, C.J. Tassone, J. Nelson Weker, M.F. Toney, T. van Buuren, M.J. Matthews, Dynamics of pore formation during laser powder bed fusion additive manufacturing, Nat. Commun. 10 (2019). https://doi.org/10.1038/s41467-019-10009-2.

[39] A. du Plessis, S.G. le Roux, Standardized X-ray tomography testing of additively manufactured parts: A round robin test, Addit. Manuf. 24 (2018) 125–136. https://doi.org/10.1016/j.addma.2018.09.014.

[40] D. Wang, C. Song, Y. Yang, Y. Bai, Investigation of crystal growth mechanism during selective laser melting and mechanical property characterization of 316L stainless steel parts, Mater. Des. 100 (2016) 291–299. https://doi.org/10.1016/j.matdes.2016.03.111.

[41] Y. Chen, S. Song, S. Zhu, X. Cui, P. Zhao, Selective laser remelting of in-situ Al2O3 particles reinforced AlSi10Mg matrix composite: Densification, microstructure and microhardness, Vacuum. 191 (2021) 110365. https://doi.org/10.1016/j.vacuum.2021.110365.

[42] B. AlMangour, D. Grzesiak, T. Borkar, J.M. Yang, Densification behavior, microstructural evolution, and mechanical properties of TiC/316L stainless steel nanocomposites fabricated by selective laser melting, Mater. Des. 138 (2018) 119–128. https://doi.org/10.1016/j.matdes.2017.10.039.

[43] X. Zhou, K. Li, D. Zhang, X. Liu, J. Ma, W. Liu, Z. Shen, Textures formed in a CoCrMo alloy by selective laser melting, J. Alloys Compd. 631 (2015) 153–164. https://doi.org/10.1016/j.jallcom.2015.01.096.

[44] J.J. Marattukalam, D. Karlsson, V. Pacheco, P. Beran, U. Wiklund, U. Jansson, B. Hjörvarsson, M. Sahlberg, The effect of laser scanning strategies on texture, mechanical properties, and site-specific grain orientation in selective laser melted 316L SS, Mater. Des. 193 (2020) 108852. https://doi.org/10.1016/j.matdes.2020.108852.

[45] J. Zhou, X. Han, H. Li, S. Liu, J. Yi, Investigation of layer-by-layer laser remelting to improve surface quality, microstructure, and mechanical properties of laser powder bed fused AlSi10Mg alloy, Mater. Des. 210 (2021) 110092. https://doi.org/10.1016/j.matdes.2021.110092.

[46] H. Chen, D. Gu, D. Dai, M. Xia, C. Ma, A novel approach to direct preparation of complete lath

martensite microstructure in tool steel by selective laser melting, Mater. Lett. 227 (2018) 128–131. https://doi.org/10.1016/j.matlet.2018.05.042.

[47] B. AlMangour, Y.K. Kim, D. Grzesiak, K.A. Lee, Novel TiB2-reinforced 316L stainless steel nanocomposites with excellent room- and high-temperature yield strength developed by additive manufacturing, Compos. Part B Eng. 156 (2019) 51–63. https://doi.org/10.1016/j.compositesb.2018.07.050.

[48] N. Hansen, Hall-petch relation and boundary strengthening, Scr. Mater. 51 (2004) 801–806. https://doi.org/10.1016/j.scriptamat.2004.06.002.

[49] P. Kürnsteiner, M.B. Wilms, A. Weisheit, P. Barriobero-Vila, E.A. Jägle, D. Raabe, Massive nanoprecipitation in an Fe-19Ni-xAl maraging steel triggered by the intrinsic heat treatment during laser metal deposition, Acta Mater. 129 (2017) 52–60. https://doi.org/10.1016/j.actamat.2017.02.069.

[50] X.P. Li, G. Ji, Z. Chen, A. Addad, Y. Wu, H.W. Wang, J. Vleugels, J. Van Humbeeck, J.P. Kruth, Selective laser melting of nano-TiB2 decorated AlSi10Mg alloy with high fracture strength and ductility, Acta Mater. 129 (2017) 183–193. https://doi.org/10.1016/j.actamat.2017.02.062.

Declaration of Competing Interest

The authors declare that they have no known competing financial interests or personal relationships that could have appeared to influence the work reported in this paper.

Highlights

- 18Ni-300 maraging steel is manufactured by a combination of selective laser melting and remelting.
- Effect of remelting with various parameters on relative density is investigated.
- Pore distributions and microstructural characteristics in different conditions are studied.
- Remelting enhances the ductility and Vickers hardness compared to as-built samples.